APPLIED SCIENCES AND ENGINEERING

Flexible elastomer patch with vertical silicon nanoneedles for intracellular and intratissue nanoinjection of biomolecules

Hyungjun Kim[1]*, Hanmin Jang[2]*, Bongjoong Kim[3]*, Min Ku Kim[1], Dae Seung Wie[3], Heung Soo Lee[2], Dong Rip Kim[2†], Chi Hwan Lee[1,3†]

Vertically ordered arrays of silicon nanoneedles (Si NNs), due to their nanoscale dimension and low cytotoxicity, could enable minimally invasive nanoinjection of biomolecules into living biological systems such as cells and tissues. Although production of these Si NNs on a bulk Si wafer has been achieved through standard nanofabrication technology, there exists a large mismatch at the interface between the rigid, flat, and opaque Si wafer and soft, curvilinear, and optically transparent biological systems. Here, we report a unique methodology that is capable of constructing vertically ordered Si NNs on a thin layer of elastomer patch to flexibly and transparently interface with biological systems. The resulting outcome provides important capabilities to form a mechanically elastic interface between Si NNs and biological systems, and simultaneously enables direct imaging of their real-time interactions under the transparent condition. We demonstrate its utility in intracellular, intradermal, and intramuscular nanoinjection of biomolecules into various kinds of biological cells and tissues at their length scales.

INTRODUCTION

The ability to introduce vertically ordered silicon nanoneedles (Si NNs) into living biological systems such as cells and tissues enables the study of biological functions and mechanisms, providing important clinical implications (*1*–*5*). Examples include nanoscale delivery of nucleic acids into cells and tissues (*6*–*8*), perturbation of cells with extracellular factors (*9*, *10*), and electrical stimulation and recording (*11*, *12*). However, these approaches remain challenging where the vertically ordered Si NNs are necessarily fabricated on a bulk Si wafer that can withstand the condition of standard nanofabrication processes (that is, high temperatures and corrosive chemicals) (*13*–*15*). The intrinsically rigid, flat, and opaque Si wafer yields a large mismatch to the soft, curvilinear, and optically transparent biological systems, limiting contact across the interface and direct observation through the substrate.

Here, we report a methodology that allows the heterogeneous integration of vertically ordered Si NNs with a thin layer of elastomer patch (herein referred to as Si NN-patch), which can provide a certain degree of mechanical flexibility, optical transparency, and cell and tissue compatibility. Both experimental and computational studies provide insight into the underlying working principle of this methodology and also suggest routes to achieving the required scalability, controllability, and reproducibility. Comprehensive demonstrations of efficient delivery of biomolecules into various living biological cells and tissues by the Si NN-patch prototype illustrate the utility of this concept.

RESULTS

Fabrication of Si NN-patch

The fabrication of the Si NN-patch begins by creating vertically ordered arrays of microscale Si pillars (initial diameter, ~3 μm) on a bulk Si wafer using the standard photolithographic patterning and deep reactive ion etching (DRIE) process (Fig. 1A, left). Subsequent steps, which include octafluorocyclobutane (C_4F_8) polymerization and DRIE process, lead to the formation of a thin passivation layer on the surface of the Si pillars in a selected manner (highlighted in yellow). A biased isotropic etching step with sulfur hexafluoride [SF_6; 85 sccm, 30 mtorr, 450-W radio frequency (RF) plasma power, 30-W platen power, 15 s] allows the creation of undercuts in the unpassivated areas of the Si pillars (Fig. 1A, middle), followed by a series of post-cleaning treatments with oxygen (O_2) plasma and piranha solution to remove the passivation layer. Immersion of the entire structure in a solution of potassium hydroxide (KOH) at 25°C leads to the reduction of the overall size of the Si pillars down to the nanometer scale (that is, Si NNs), which can simultaneously form a tapered angle at the undercut areas (Fig. 1A, right). Details of the fabrication procedures can be found in Materials and methods.

The next step is performed by using a transfer printing method to physically liberate the as-prepared vertical Si NNs from the bulk Si wafer and then to partly embed them into a silicone elastomer, such as polydimethylsiloxane (PDMS). The transfer printing process begins by placing a spin-casted, partly cured layer of PDMS at the top portion of the as-prepared Si NNs, where an air gap can exist between the PDMS layer and the Si wafer (Fig. 1B, left). A subsequent annealing step at 130°C for 10 min facilitates the completion of the polymerization of the PDMS layer. Immersion of the entire structure in a solvent solution such as hexane and dichloromethane allows PDMS to swell and to expand its volume up to >230% within ~2 min (movie S1) (*16*). PDMS undergoes time-dependent nonhomogeneous morphological expansion, causing a traveling wave of mechanical deformations such as bending and twisting to propagate all around and entirely through the substrate (*17*). The expansion of PDMS can generate cracks localized at the undercut areas of Si NNs, where the most substantial mechanical stress is concentrated. This controlled cracking phenomenon results in the physical separation of Si NNs from the bulk Si wafer (Fig. 1B, middle). Dehydration of the resulting structure in a convection oven at 70°C for ~1 hour allows the PDMS substrate to recover its original volume

[1]Weldon School of Biomedical Engineering, Purdue University, West Lafayette, IN 47907, USA. [2]School of Mechanical Engineering, Hanyang University, Seoul 04763, South Korea. [3]School of Mechanical Engineering, Purdue University, West Lafayette, IN 47907, USA.
*These authors contributed equally to this work.
†Corresponding author. Email: dongrip@hanyang.ac.kr (D.R.K.); lee2270@purdue.edu (C.H.L.)

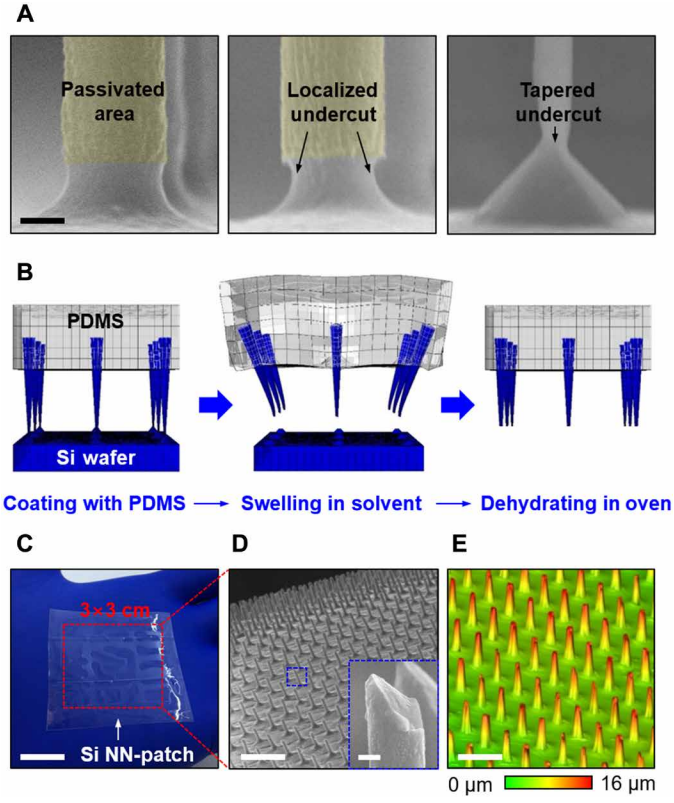

Fig. 1. Images and illustrations for the integration of vertically ordered Si NNs onto an elastomer patch. (**A**) A series of scanning electron microscopy (SEM) images of vertically ordered Si pillars with selected passivation layer (left), with localized undercut (middle), and after the size is reduced down to the nanoscale (right). Scale bar, 1 μm. (**B**) Schematic illustrations of the key steps to physically liberate Si NNs from their native Si wafer via the swelling of PDMS. (**C**) Optical image of a representative Si NN-patch. Scale bar, 1.5 cm. (**D**) Magnified SEM image of the partly embedded Si NNs into PDMS. The inset highlights the needle-like sharp tips. Scale bars, 20 μm and 600 nm (inset). (**E**) Confocal laser scanning microscopy (CLSM) image of Si NNs. Scale bar, 30 μm.

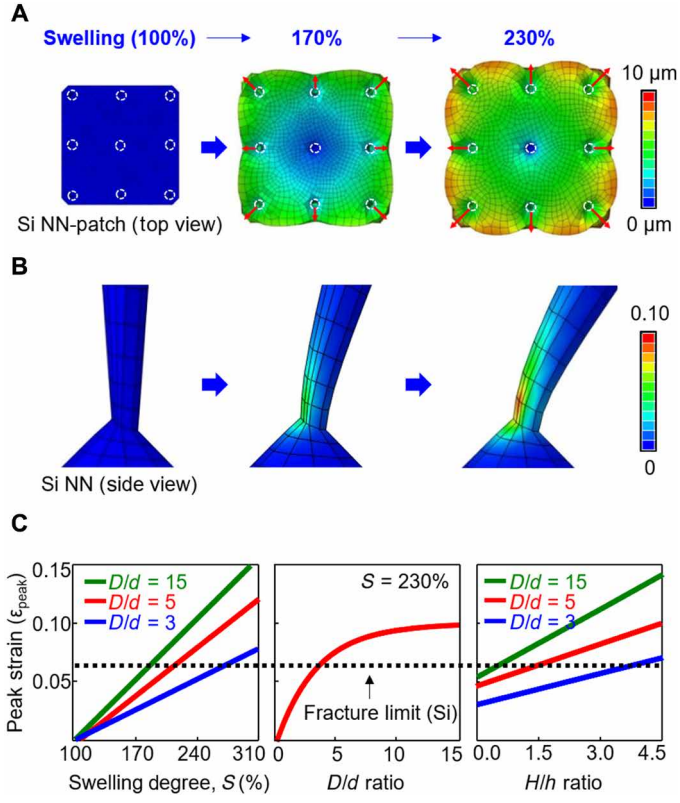

Fig. 2. Mechanism study and mechanical analysis for controlled cracking of Si NNs. (**A**) FEA results of displacement of PDMS under swelling at 100, 170, and 230%. (**B**) Corresponding FEA results of maximum principal strain distributions along a single Si NN during each swelling condition. (**C**) Computational data showing the effect of peak strain (ε_{peak}) on *S* (left), *D*/*d* ratio (middle), and *H*/*h* ratio (right). Black dashed line denotes a theoretical fracture limit of the Si NN.

(Fig. 1B, right). The thickness of the PDMS substrate can then be reduced by floating it on the surface of a wet etchant such as tetra-*n*-butylammonium fluoride (TBAF; Sigma-Aldrich), followed by thorough washing with distilled (DI) water. Details of the transfer printing process can be found in Materials and methods.

Figure 1C shows an optical image of a representative Si NN-patch that includes an array (3 cm × 3 cm) of vertically ordered Si NNs on a sheet of PDMS. The enlarged SEM image (Fig. 1D) confirms that the original geometry, gap distance, and vertical arrangement of Si NNs are maintained with high fidelity after the transfer printing process. The inset image highlights the needle-like sharp tip of Si NNs that can minimize the potential damage of living biological systems during nanoinjection (*18*). Figure 1E shows a representative confocal CLSM image, indicating that the transferred Si NNs on the PDMS substrate have a uniform height. It also appears that the fractured planes on both the donor Si wafer and the receiver PDMS substrate are uniform across the entire area (fig. S1). The overall size of Si NNs can be varied to optimize the features required for the envisioned intracellular and intratissue nanoinjections at various length scales. Here, a specific range of tip diameter (80 nm to 3 μm) and height (8 to 70 μm) of Si NNs with approximate aspect ratios of 2:1 to 125:1, which can be used for different sizes of cells or tissues, was demonstrated (fig. S2). It is noted that no substantial change in mechanical properties, such as Young's modulus of the PDMS substrate by the load of Si NNs, exists.

Mechanism study and mechanical analysis for controlled cracking of Si NNs

Understanding the underlying mechanism of the controlled cracking of Si NNs is essential to achieve the required scalability, controllability, and reproducibility of the transfer printing process. Figure 2A provides finite element analysis (FEA) results of the displacement for a simplified test bed structure that is composed of an array (3 cm × 3 cm) of Si NNs (white circular marks) built on a PDMS substrate under swelling (*S*) at 100% (left), 170% (middle), and 230% (right) relative to its original volume while assuming that the PDMS substrate swells homogeneously with time (see movie S2 for the continuously captured images). The deformation of Si NNs is modeled by linear elastic behavior, with Young's modulus (*E*) of 112.4 GPa, diameter of Si NNs (*D*) of 3 μm, diameter of undercut area (*d*) of 0.2 μm, height of Si NNs (*H*) of 20 μm, and protruding height of Si NNs out of the PDMS substrate (*h*) of 6 μm. A schematic illustration displaying the modeling geometry and boundary conditions is shown in fig. S3A.

Figure 2B shows the strain distribution (ε) of a single Si NN under each swelling condition, revealing that the peak principal strain (ε_{peak}) exists in the undercut area, where the maximum magnitude, at $S = 230\%$, exceeds, by >12%, its fracture limit (~5%) (*19*, *20*). The induced peak strain can lead to the physical separation of Si NNs from the bulk Si wafer, as also observed in the experimental results described above.

Figure 2C shows a summary of computational (FEA) result, which reveals the effects of several important parameters such as *S*, *D*/*d* ratio, and *H*/*h* ratio on the peak strain localized at the undercut area. The theoretical curve (black dashed line) defines the fracture limit of the Si NN, where any deviation above this curve implies potential fractures. The results indicate that the peak strain increases linearly as the PDMS substrate expands in volume (left graph), in which it rises rapidly at small *D*/*d* and then gradually reaches steady state as the *D*/*d* ratio becomes larger (middle graph). The increase of *H*/*h* ratio leads to the elevation of the peak strain at the undercut area (right graph). For comparison, the corresponding computational results (FEA) of the strain distributions in variously controlled conditions are summarized in fig. S3B. The effect of different solvent solutions, including ethanol ($S = 110\%$), hexane ($S = 230\%$), and dichloromethane ($S = 280\%$), on the peak strains is shown in fig. S4. These results provide essential information not only to optimize the design of Si NNs but also to specify operational parameters for achieving the controlled cracking process.

Cell compatibility and minimal invasiveness of Si NN-patch

Cell compatibility is a critical consideration for the implementation of the Si NN-patch in many envisioned intracellular applications. Figure 3A shows the result of a cell compatibility assay by using the Si NN-patch that is seeded with human dermal fibroblast (HDF) cells in a culture medium [Fibroblast Basal Medium, American Type Culture Collection (ATCC)]. This setup (that is, Si NNs at the bottom) allows the cells to progressively enter into Si NNs within 1 hour (*21*). The result obtained from a colorimetric kit [MTT (3-(4,5-dimethylthiazol-2-yl)-2,5-diphenyltetrazolium bromide), Sigma-Aldrich] indicates that the proliferation rate of the cells is consistently increased throughout the assay period (72 hours), providing no substantial difference when compared with that of control Si NNs built on a Si wafer (red bars) and a bare Si wafer without Si NNs (yellow bars). Details of the cell culture and associated experimental procedures can be found in Materials and methods.

To determine post-nanoinjection damage to cells, we conducted further tests by pressing the Si NN-patch onto HDF cells with a centrifuge at 500 rpm for 1 min (ALC PM140 centrifuge, Thermo Fisher Scientific). This setup (that is, Si NNs on top) allows Si NNs to be immediately injected into the cell membrane (*7*). Figure 3B shows the experimental results obtained from a lactate dehydrogenase (LDH) assay (Abcam) by using the Si NN-patch (green bars), control Si NNs built on a Si wafer (red bars), and a bare Si wafer without Si NNs (yellow bars) at assay periods of 24 and 48 hours. As a positive control, approximately 2.5 μl of Triton X-100 [0.25% (v/v); Sigma-Aldrich] is introduced in the culture medium to the HDF cells (blue bars). The results show that the concentration of LDH in the medium remains well maintained for all of these cases, implying that no substantial leakage of intracellular materials such as LDH occurs throughout the immediate nanoinjection of the Si NN-patch.

Intracellular nanoinjection of Si NN-patch

The key benefit of the Si NN-patch, especially when coupled with actively moving biological cells, arises from its ability to form a mechanically elastic interface between Si NNs and biological cells. For instance, the soft PDMS substrate ($E \approx 2$ MPa) deforms elastically to accommodate the mechanical strains induced by cell behaviors such as adhesion, spreading, migration, and proliferation, while the stiff Si NNs ($E \approx 112.4$ GPa) undergo negligible deformation. Figure 3C shows an example by using the Si NN-patch interfaced with MCF7 cells, displaying that the cells spread well to bridge over the gaps between adjacent Si NNs and induce the elongation of filopodia. Notably, the PDMS substrate deforms elastically to accommodate the strain induced by the cells, allowing Si NNs to lean toward cells without any mechanical buckling or fracture (marked with red arrows). These interactions are markedly distinct from those observed by using conventional Si NNs built on a bulk Si wafer, in which Si NNs are either buckled out of plane or fractured when deformed beyond the fracture limit (*22*–*24*), as also experimentally reproduced in fig. S5. Control experiments on dissimilar kinds of cells such as SKOV3 and HDF by using different sizes of Si NNs produce consistent results (fig. S6), confirming that the elastomer substrate is effective in preventing the mechanical buckling or fracture of Si NNs by natural behaviors of the cells.

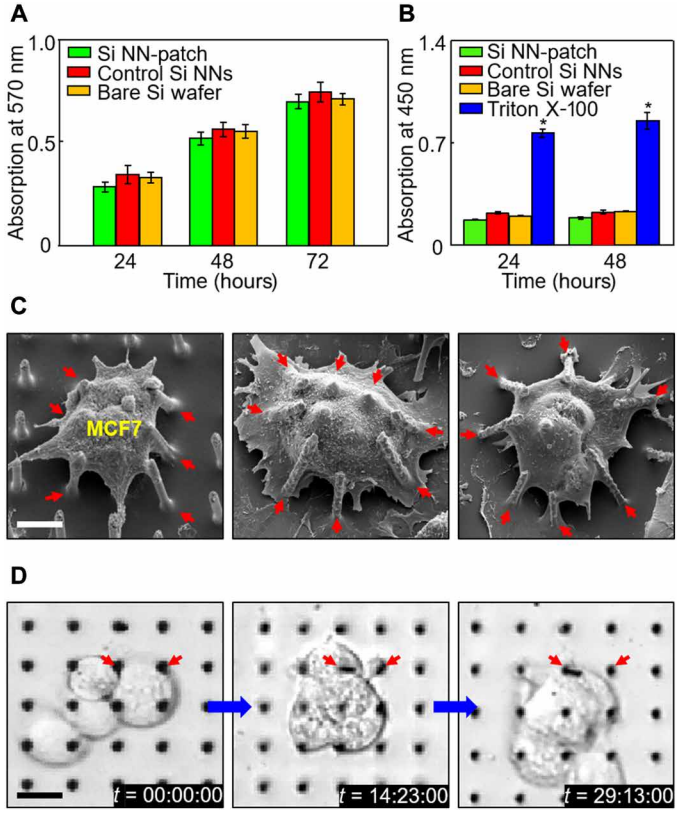

Fig. 3. Basic characterizations of Si NN-patch. (**A**) Results of MTT assay in the cytotoxicity tests of HDF cells interfaced with the Si NN-patch (green) and control Si NNs on a Si wafer (red) and a bare Si wafer (yellow). Error bar represents the SD of three replicates. (**B**) Results of LDH assay in the invasiveness tests of HDF cells for 2 days. Triton X-100 is used as a positive control (blue). Error bar represents the SD of three replicates. (**C**) SEM images of MCF7 cells on a representative Si NN-patch at 24 hours after nanoinjection. Scale bar, 10 μm. Arrows highlight the deformed Si NNs by cell deformations. (**D**) Time-lapsed live differential interference contrast (DIC) images of HDF cells that interacted with Si NNs at the bottom. Scale bar, 10 μm.

Another unique feature of the Si NN-patch includes its optical transparency (~90%), enabling the direct, real-time observation of unstrained biological cells during/after nanoinjection. Figure 3D shows an example of a DIC microscopy (A1Rsi confocal microscope, Nikon) image of MCF7 cells interfaced with Si NNs, captured from a continuously recorded movie for 36 hours (movie S3). This enhanced observation confirms the following details: (i) The induced forces by the cells tend to bend Si NNs toward the cells (marked with red arrows), (ii) the cellular protrusions such as lamellipodia become focused near boundaries between the cells and Si NNs, and (iii) the cells remain viable for the entire period of intracellular nanoinjection of Si NNs, exhibiting continued cell adhesion, spread, migration, and proliferation. Further investigations to understand how various types of cells would respond to Si NNs that can be incorporated with drugs, genes, or proteins of particular interest would be possible with this Si NN-patch platform. To demonstrate this possibility, we showed several experimental demonstrations in the following sections.

Nanoscale surface pores for improved loading capacity of biomolecules

The formation of nanoscale pores on the surface of Si NNs leads to a substantial increase of the surface area, thereby improving the loading capacity of biomolecules (*7*). The formation process, which relies on the conventional metal-assisted chemical etching (MACE) method (*25*), occurs by immersing the as-prepared Si NNs on a bulk Si wafer in a mixed solution of catalytic silver (Ag) nanoparticles and etchants for a prescribed time period until the desired pore volume is achieved (Fig. 4A). The measured diameter and porosity (surface fraction) of the nanopores ranged from 8.5 nm to 19.4 nm and from 32.9% to 52.1%, respectively, when the processing time for MACE is varied from 5 to 30 s. Details of the MACE procedures can be found in Materials and methods. Figure 4B shows representative fluorescence microscopy images of Si NNs with (left) and without (right) the nanopores on the surface by using a green fluorescein isothiocyanate (FITC) dye (Sigma-Aldrich). For comparison, representative SEM images of the control Si NNs without the nanopores appear in fig. S7. The results show that the most substantial fluorescence intensity appears at the nanoporous surfaces of Si NNs, whereas the exact opposite occurs in the control Si NNs. Further tests using model nucleic acids such as small interfering RNA (siRNA) labeled with Cy3 (red color) produce consistent results (Fig. 4C). The nanoscale pores on the surface of Si NNs contribute to a large loading capacity of biomolecules.

To demonstrate its utility in intracellular delivery of biomolecules, we introduced the nanoporous Si NNs loaded with Cy3-siRNAs into model living cells, such as green fluorescent protein (GFP)–expressed MCF7 cells. The confocal microscopy images (fig. S8) present examples of the cells cultured by both seeding the cells on Si NNs (that is, Si NNs at the bottom) and pressing Si NNs on top at 500 rpm for 1 min (that is, Si NNs on top). The results show that multiple numbers of Si NNs are introduced into a single cell in a spatially distributed manner without any substantial physical damage or cell rupture. It is also observed that the siRNAs are evenly diffused within the cytosol of the cells at 24 hours after nanoinjection, as evidenced in the confocal microscopy image (Fig. 4D), where yellow appears uniform by combining GFP-MCF7 (green) and Cy3-siRNAs (red). Figure 4E shows the results of a fluorescence-activated cell sorting (FACS) analysis with SKOV3 cells, indicating that the transfection efficacy of siRNAs was >95% within 24 hours after nanoinjection. The corresponding efficacy in silencing housekeeping genes such as glyceraldehyde-3-phosphate-dehydrogenase (GAPDH) of the cells was >80% ($P < 0.0001$; Fig. 4F). It is also noted that no siRNA silencing effect occurs in both the control nanoinjection of scrambled siRNAs and the treatment of the cells in the siRNA solution (fig. S9).

Intratissue nanoinjection of Si NN-patch

The Si NN-patch, due to its thin and flexible properties, provides the ability to intimately contact onto the curvilinear, actively moving surface of living biological tissues such as skins and muscles. This feature is particularly important in the implementation of the Si NN-patch in intradermal and intramuscular delivery of biomolecules. To demonstrate this, we performed a set of in vivo evaluations by using a tailored size (1 cm by 1 cm) of the Si NN-patch for an athymic nude mice model (n = 10, 6 weeks old, NCr-Fox1nu, Charles River Laboratories). The Si NN-patch is composed of nanoscale pores on the surface that are incorporated with a fluorescent dye (DyLight 800, Pierce Thermo Scientific) as a surrogate of

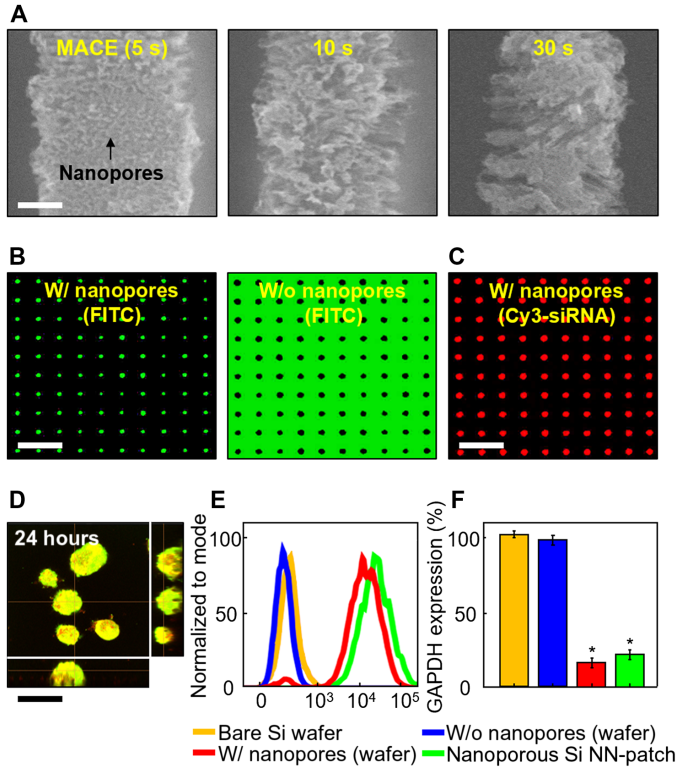

Fig. 4. Formation of nanoscale surface pores and intracellular nanoinjection of siRNA. (**A**) SEM images of nanopores formed on the surface of Si NNs at different treatment times of MACE. Scale bar, 250 nm. (**B**) Confocal microscopy images of Si NNs with (left) and without (right) nanopores on the surface by using a green fluorescence dye. Scale bar, 15 μm. (**C**) Confocal microscopy image of nanoporous Si NNs loaded with Cy3-siRNAs (red). Scale bar, 15 μm. (**D**) Confocal microscopy image of GFP-MCF7 cells at 24 hours after nanoinjection of Cy3-siRNAs. Scale bar, 15 μm. (**E**) Results of flow cytometry (FACS) analysis for SKOV3 cells at 48 hours after nanoinjection of Cy3-siRNAs by using the nanoporous Si NN-patch (green) and control Si NNs on a bulk Si wafer with (red) and without (blue) nanopores on the surface and a bare Si wafer (yellow). (**F**) Corresponding results of GAPDH analysis for the SKOV3 cells. Error bar represents the SD of three replicates.

small-molecule drugs. Figure 5A shows optical images of the Si NN-patch that is placed on the skin (left image) and subcutaneous muscle (middle image) of the mice for intradermal and intramuscular nanoinjections, respectively. For comparison, a control experiment (right image), which exhibits a large morphological mismatch between the curved parts (for example, spinal sections) of the body and the bulk Si wafer, was performed by using conventional Si NNs built on a bulk Si wafer. The results show that the flexible Si NN-patch is capable of intimately interfacing with the skin in a manner that can minimize mechanical constraints on natural body motions of the mice awake (movie S4). The interfacial contact between the Si NN-patch and the skin was durable for a long period of time (days) without any evidence of delamination, unless the mice tear the Si NN-patch off by themselves. In addition, the mice implanted with the flexible Si NN-patch on the subcutaneous muscle showed normal behaviors (movie S5). Figure 5B shows the corresponding IVIS images, highlighting that the small-molecule dyes are uniformly distributed and diffused across the curved spinal regions of the mice, followed by complete absorption throughout the body. These results demonstrate its potential utility in efficient intratissue nanoinjection of biomolecules into living animals.

In vivo tissue compatibility of Si NN-patch

In vivo tissue compatibility of the Si NN-patch in both skin-wearable and implantable scenarios is evaluated. Figure 6A shows real-time bioluminescence images of the mice interfaced with the Si NN-patch (left) and conventional Si NNs on a bulk Si wafer (middle) and control treatment (right) of phorbol 12-myristate 13-acetate (PMA; 1 mM, ~20 μl; Sigma-Aldrich) at 5 hours following the implementation. The results show that no inflammation occurs in the implemented sites of the skin, subcutaneous muscle, and ear upon systemic administration of luminol (5-amino-2,3-dihydro-1,4-phthalazinedione), whereas acute inflammation appears widespread in the PMA-treated mice. Hematoxylin and eosin (H&E) histological cross-sectional views of the treated tissue sections (Fig. 6B) produce substantial similarity with intact tissues and no signs of epidermal, dermal, or capillary vessel disruption. Together, these findings suggest that the Si NN-patch can be considered as compatible for integration onto the skin and subcutaneous muscle. It is noted that Si-based nanomaterials are dissolvable in physiological circumstances, following a complete harmless resorption in the body (*26*–*29*). Here, the measured dissolution rates of representative nanoporous Si NNs were ~6 and ~68 nm/day in phosphate-buffered saline (PBS) at 37°C with pH values of 7.4 and 10.0, respectively (fig. S10).

DISCUSSION

Development of a high-fidelity transfer printing method by using a controlled cracking phenomenon enables the heterogeneous integration of vertically ordered Si NNs onto a thin sheet of elastomer

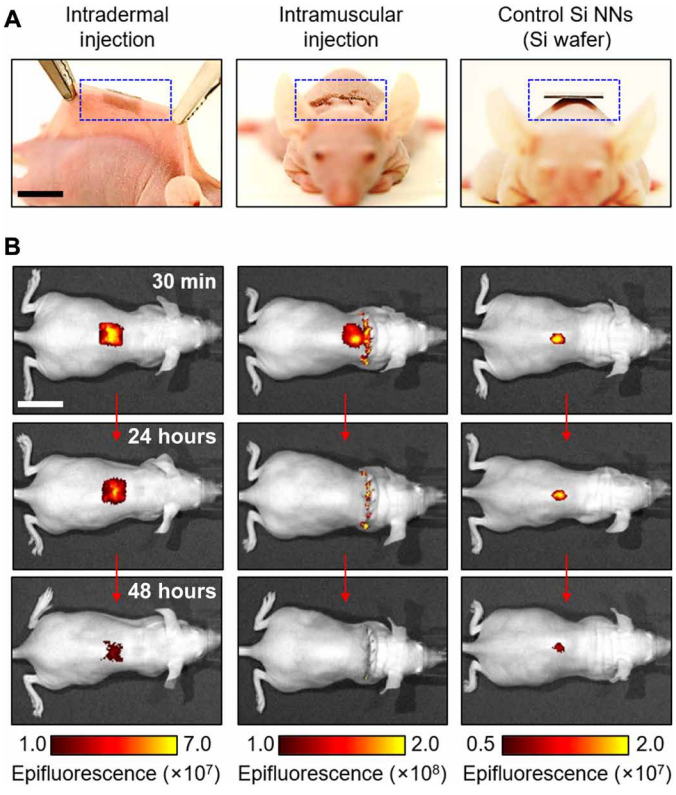

Fig. 5. Intratissue nanoinjection of Si NN-patch. (**A**) Optical images of the mice interfaced with the Si NN-patch for intradermal (left) and intramuscular (middle) nanoinjection. Scale bar, 1 cm. Conventional Si NNs built on a bulk Si wafer are used for control comparison (right). (**B**) Corresponding IVIS images of the mice for up to 48 hours after nanoinjection. Scale bar, 2 cm.

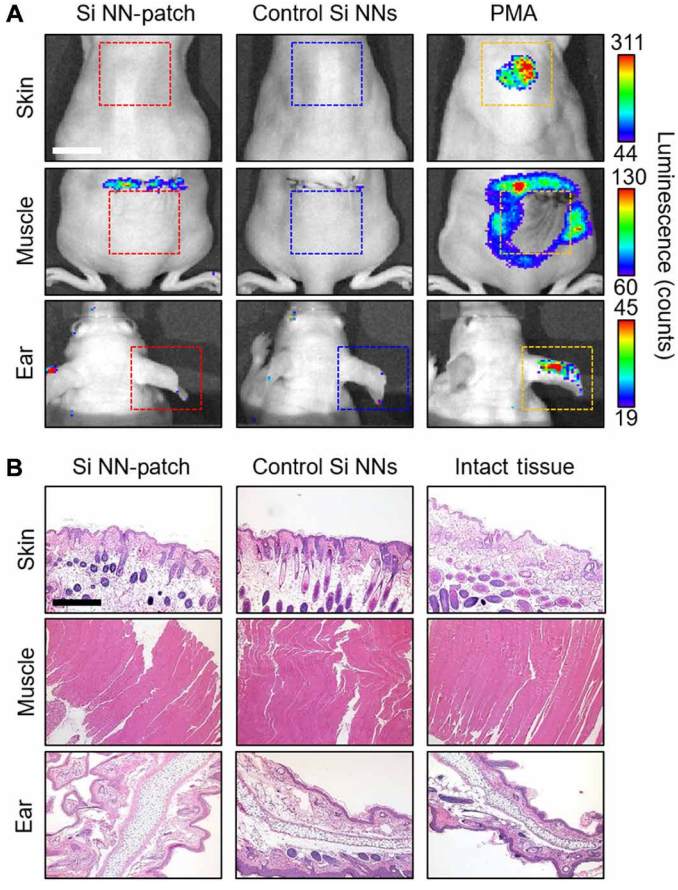

Fig. 6. In vivo tissue compatibility of Si NN-patch. (**A**) Real-time bioluminescence images on the skin, muscle, and ear of the mice at 5 hours following the implementation of the Si NN-patch (left column) and control Si NNs (middle column) and with control PMA treatment (right column). Scale bar, 10 mm. (**B**) Corresponding H&E histological cross-sectional views of the treated tissue sections. Scale bar, 400 μm.

patch. Si NNs are made of monocrystalline grade Si at the nanoscale by using an existing Si nanofabrication technology, creating tip diameters of 80 nm to 3 μm and surface pore sizes of 5 to 19 nm in this study. Because of its mechanical flexibility, cell and tissue compatibility, and nanoscale controllability, the resulting outcome can form an effective interface between Si NNs and various biological systems, enabling high-efficacy nanoinjection of biomolecules. In addition, the optical transparency of the Si NN-patch enables simultaneous, real-time observation of unstrained cells during their interactions with Si NNs. We anticipate that this platform will affect a broad range of efforts in intracellular and/or intratissue communications, with potential applications in the areas of cell and systems biology, drug discovery, and cellular detection and manipulation. Further investigations to evaluate the therapeutic effects of the drug/gene delivery would be important to confirm the utility of the Si NN-patch.

MATERIALS AND METHODS

FEA method

To understand the underlying mechanics of PDMS and Si NNs under mechanical deformations, we conducted this study using the ABAQUS/standard package. The deformations of PDMS and Si NNs were modeled by linear elastic behavior with Young's modulus (E) of 2 MPa and 112.4 GPa, respectively (*30*, *31*). The PDMS substrate was modeled by C3D8T (coupled displacement-temperature 8 nodes solid elements), while Si NNs were modeled by C3D8R (8 nodes linear brick, reduced integration solid elements) with predefined boundary conditions.

Fabrication of Si NNs with undercut on a bulk Si wafer

The fabrication of Si NNs began with the immersion of a bulk Si wafer (p-type, 525 μm thick, 0 to 100 ohm·cm) in a buffered oxide etch (J. T. Baker Inc., USA) solution for 1 min to remove the native oxide layer on the surface. Standard photolithographic patterning and anisotropic DRIE allowed the creation of arrays of vertical Si pillars with the predefined diameter and aspect ratio. A deposition step was conducted to passivate the surface of the Si pillars with a thin layer of the $(C_xF_y)_n$ polymer using C_4F_8 gas with a flow rate of 130 sccm under an RF plasma power of 800 W, followed by an etching step using SF_6 gas with a flow rate of 85 sccm under an RF plasma power of 450 W and a platen power of 12 W. Following an additional DRIE to expose the bottom areas of the Si pillars, a biased isotropic etching step was conducted to form undercuts selectively at the exposed areas using SF_6 gas with a flow rate of 85 sccm under an RF plasma power of 450 W and a platen power of 30 W. The remaining passivation layer was removed by using standard O_2 plasma treatment (20 sccm, 150 W, 50 mtorr, 15 min) and piranha cleaning (75% H_2SO_4 and 25% H_2O_2). The entire structure was immersed in a solution of 13 weight % (wt %) KOH (Fisher Scientific, USA) at 25°C to reduce the overall size of the Si micropillars down to the nanoscale (~80 nm in the minimum tip size). The as-prepared vertical Si NNs were then physically separated from the fabrication of a Si wafer and transferred to a thin layer of PDMS (details in the following section). The control Si NNs were prepared separately on a Si wafer using similar fabrication procedures but without the last transfer step. A standard isotropic etching step was used to form the sharp tip of Si NNs on a Si wafer under an RF plasma power of 450 W and a platen power of 0 W.

Transfer printing process

The process began with the preparation of a PDMS substrate (Sylgard 184, $E \approx 2$ MPa, initial thickness ≈ 250 μm) by mixing the base material and curing agent with a ratio of 10:1 by weight, followed by spin-casting at 100 rpm for 10 min and complete polymerization at 70°C for 2 hours. The PDMS substrate was then coated with another thin layer of spin-casted (1000 to 2000 rpm for 10 min), partly cured (at room temperature for 3 min) PDMS to serve as an adhesive, where the as-prepared Si NNs with undercuts on a Si wafer were placed upside down. At this stage, the thickness of the adhesive layer was controlled during the spin-casting process to determine the protruding height of Si NNs out of PDMS. A subsequent thermal annealing was conducted at 130°C for 10 min to complete the polymerization of the adhesive layer and secure the physical bonding with the surrounding Si NNs as well as the PDMS substrate at the bottom. Immersion of the entire structure in a solvent, such as hexane (20 ml; Fisher Scientific, USA), allowed the PDMS substrate to expand its volume up to >200% within 2 min and to liberate Si NNs from the Si wafer via cracking at the undercut areas. The resulting structure was thoroughly washed with DI water and dehydrated in a convection oven at 70°C for ~1 hour to remove the absorbed solvent, which allowed the PDMS substrate to shrink and recover its original volume. The thickness of the PDMS layer can then be reduced by floating it on a mixed etchant of 9 volume % TBAF (75 wt % in H_2O; Sigma-Aldrich, USA) and 91 volume % acetone at an etch rate of 10 μm/min at room temperature. The thickness of the resulting PDMS substrate used in this study ranged from 80 to 280 μm.

Formation of nanoscale pores on the surface of Si NNs

MACE of Si NNs was conducted in a mixed solution of 20 mM silver nitrate ($AgNO_3$; Sigma-Aldrich, USA) and concentrated hydrofluoric acid (49%; J. T. Baker Inc., USA) to form nanoscale pores on the surface. The porosity was tuned by adjusting the molarity of solutions, doping concentration of Si NNs, temperature, and etching time (*25*). The finished structure was then immersed in a solution of Ag etchant (TFS, KI-I_2 complex liquid, Transene Inc., USA) for ~1 min to eliminate the Ag residues on the surface of Si NNs. The nanoscale pores on the surface of Si NNs were inspected with a high-resolution SEM (S-4800, Hitachi, Japan).

Intracellular nanoinjection and siRNA delivery

To evaluate the efficacy in intracellular nanoinjection and siRNA delivery, the established Si NN-patch was tested on a range of biological cells including breast cancer cells (MCF7, ATCC, USA), human dermal fibroblasts (HDF, ATCC, USA), and ovarian carcinoma cells (SKOV3, ATCC, USA). For these tests, a test bed Si NN-patch was sterilized in 70% (v/v) ethanol for 30 min, washed twice in PBS (Gibco, USA), and dried under ultraviolet (UV) irradiation for 1 hour. The Si NN-patch was then immersed in a solution of 2% 3-aminopropyltriethoxysilane (Sigma-Aldrich, USA) for 2 hours to functionalize the surface of Si NNs and capture nucleic acids (Cy3-siRNA, Invitrogen, USA). The sequences for the siRNA used in this study are as follows: 5′-GGAGCAGUUUGAAUGUCCAtt-3′ (sense) and 5′-UGGACAUUCAAACUGCUCCga-3′ (antisense). Following rinsing with PBS, the cells were interfaced with the Si NN-patch either by seeding them over Si NNs (that is, Si NNs at the bottom) or by pressing the Si NN-patch over cells with centrifugal force at 500 rpm for 1 min (that is, Si NNs on top).

Analysis of cells after nanoinjection

For the MTT assay, approximately 5×10^4 cells were seeded on a test bed Si NN-patch in a 24-well plate. At each measurement point, 200 μl of MTT solution was added to the wells and incubated for 4 hours. The cell medium was excavated, and 400 μl of dimethyl sulfoxide (Sigma-Aldrich, USA) was added to dissolve precipitated formazan. Approximately 100 ml of the solution was transferred to a 96-well plate and measured with a microplate reader (SpectraMax Plus 384 reader, Molecular Devices, USA) at 570 nm. For the LDH assay, the cells were evaluated at 24 and 48 hours after treatment of 0.25% (v/v) Triton X-100 (Sigma-Aldrich, USA) as a positive control. After incubation, 100 ml of supernatant from each well was removed and centrifuged at 1000 rpm for 5 min. Ten microliters of aliquot was transferred to additional microplate, and 100 μl of LDH assay buffer mix was added to the wells and incubated for 30 min. The absorbance was measured with a microplate reader (SpectraMax Plus 384 reader, Molecular Devices, USA) at 450 nm. For the confocal microscopy analysis, the cells were fixed with 4% (v/v) paraformaldehyde (Sigma-Aldrich, USA) in PBS for 15 min, stained with 4′,6-diamidino-2-phenylindole (500 nM, Fisher Scientific, USA) for 2 min, and then mounted with an antifade reagent (Gold Antifade Mountant, Invitrogen, USA). For the flow cytometry (FACS) analysis, the cells injected with GAPDH Cy3-siRNAs were trypsinized, washed several times with PBS, and then fixed in 0.5% (v/v) paraformaldehyde for 1 hour. To confirm the expression of GAPDH, approximately 3×10^4 cells were seeded on a 12-well plate and incubated for 24 hours. The efficacy in silencing GAPDH was evaluated by analyzing fluorescent intensity at 450 nm with a standard GAPDH assay kit (Abcam, USA).

Flow cytometry analysis

For flow cytometry (FACS) analysis, cells with Cy3-siRNA-GAPDH were trypsinized, collected in a microcentrifuge tube (1 ml), centrifuged at 300 rpm, washed twice with PBS, and then fixed in 0.5% (v/v) paraformaldehyde for 1 hour. Cell clumps were removed by filtering through 40 μm of a mesh (Falcon Cell Strainers, Thermo Fisher Scientific, USA). The specimens were analyzed on the Fortessa Flow Cytometer (GE Healthcare, USA) equipped with lasers (405, 488, 561 and 635 nm) and emission filters for phycoerythrin (long pass, –; band pass, 582/15). At least 10,000 cells were analyzed per specimen. All data were processed with FlowJo software (TreeStar Inc., USA).

In vivo animal tests

All animal protocols and experiments were in accordance with the Purdue Animal Care and Use Committee (protocol number: 1612001512) and conducted in compliance to applicable regulations. As a model system, athymic nude mice (n = 10, 6 weeks old, NCr-Fox1nu, Charles River Laboratories, USA) were used in the in vivo animal tests. The Si NN-patch was sterilized with 70% ethanol, exposed to UV light for 30 min, and then immersed in a DyLight 800 dye (1 μl/ml; Thermo Fisher Scientific, USA) for 5 min. For the transdermal nanoinjection, the Si NN-patch was gently placed on the skin of mice awake with a medical-grade adhesive (Roll-On Adhesive, JOBST, USA) and pressed firmly for ~10 s. The behavior of the mice was monitored in real time and recorded with a high-resolution video camera (EOS 700D, Canon Inc.). For the intramuscular nanoinjection, the mice were anesthetized with avertin (Sigma-Aldrich, USA) by intraperitoneal nanoinjection at a dose of 250 mg/kg, followed by careful incision of the skin with surgical scissors to expose the gluteal and lumbar muscles. In these tests, the incision was made on the upper back of the mice, where the Si NN-patch was inserted. The incisional site was then sutured using surgical needle and thread. To induce acute inflammation, PMA (100 μM, 40 μl; Sigma-Aldrich, USA) as a positive control was rubbed on the skin, muscle, and ear. After ~5 hours of implementations, 100 μl of luminol (body weight, 200 mg/kg; Sigma-Aldrich, USA) was administered by intraperitoneal nanoinjection, and then the mice were imaged (exposure time, 3 min; binning, 4). For the histological examination, approximately 4 μm of tissue section was cut, fixed in 10% formalin (Sigma-Aldrich, USA) for 24 hours, and then stained with H&E (Sigma-Aldrich, USA) using a light microscope (Eclipse 90i, Nikon Inc.).

IVIS imaging

For IVIS analysis, the Si NN-patch loaded with a DyLight 800 dye was placed either on the top of the skin or under the skin of mice and then gently pressed with thumb, with minimal movement of the Si NN-patch for at least 1 min. The Si NN-patch was removed and washed twice with PBS. Mice were anesthetized with inhaled isoflurane anesthesia with a Classic T3 isoflurane vaporizer (Smith Medical, Dublin, OH) and exposed to 2.5% isoflurane delivered in O_2 (2 liters/min) within a 1-liter induction chamber. The fluorescence of injection site was measured with an IVIS Lumina II imaging system (Caliper Life Sciences, USA) at 30 min, 24 hours, and 48 hours, with an exposure time of 1 s each with a 150-W quartz halogen lamp, and was filtered using an indocyanine green (ICG) excitation filter (wavelength, 710 to 760 nm) and an ICG emission filter (wavelength, 810 to 875 nm). Data analysis was performed with Living Image software (version 4.4, PerkinElmer Inc.).

Bioluminescence imaging

For bioluminescence imaging analysis, luminol sodium salt (~200 mg/kg; Sigma-Aldrich, USA) was injected to the mice via an intraperitoneal injection. Then, the mice were placed on a warmed stage inside a light-tight camera box and anesthetized with compressed air containing 2.5% isoflurane with a Classic T3 isoflurane vaporizer (Smith Medical, Dublin, OH). Bioluminescence images were acquired with an IVIS Lumina II imaging system (Caliper Life Sciences, USA) for 3 min of the exposure time, with F/stop = 1 and binning = 4.

SUPPLEMENTARY MATERIALS

Supplementary material for this article is available at http://advances.sciencemag.org/cgi/content/full/4/11/eaau6972/DC1

Fig. S1. SEM images (scale bar, 10 μm) of the donor Si wafer and the receiver PDMS substrate after the physical separation process, with their enlarged images (scale bar, 1 μm).

Fig. S2. SEM images of Si NNs with varied tip size and height.

Fig. S3. Schematic illustration for modeling geometry and boundary conditions and computational results (FEA) of strain distributions of a single Si NN under deformations at varied D/d ratio, h, and S.

Fig. S4. Computational (FEA) data showing the effect of peak strain (ε_{peak}) on D/d ratio and H/h ratio using dichloromethane (green), hexane (red), and ethanol (blue).

Fig. S5. SEM images (scale bars, 7, 5, and 3 μm from the top) of cells interfaced with control Si NNs built on a bulk Si wafer.

Fig. S6. SEM images (scale bars, 7 and 10 μm from the left) of SKOV3 cells (left) and HDF cells (right) interfaced with different sizes of Si NNs at the bottom.

Fig. S7. SEM images (scale bars, 5 and 1.5 μm from the left) of control Si NNs without the nanoscale pores on the surface.

Fig. S8. Confocal microscopy images (scale bar, 10 μm) of the cultured MCF7 cells at 30 min after nanoinjection by either pressing Si NNs on top (left) or seeding the cells on Si NNs (right).

Fig. S9. Measured GAPDH expression by a control nanoinjection of scrambled siRNAs (left) and a control treatment in the siRNA solution (right).
Fig. S10. Dissolved diameter (D/D_0 ratio) of nanoporous Si NNs in a PBS solution with pH values of 7.4 (red) and 10 (blue) at 37.5°C.
Movie S1. An experimental demonstration (scale bar, 2.5 mm; 20× speed) showing the expansion of PDMS when soaked in hexane.
Movie S2. FEA results of displacement for a simplified structure that includes an array (3 cm × 3 cm) of Si NNs on a thin layer of PDMS under the expansion up to 230% in volume.
Movie S3. Continuously recorded live DIC image (scale bar, 15 μm; 4000× speed) of MCF7 cells for 36 hours.
Movie S4. A continuously recorded movie (scale bar, 2 cm; 1× speed) showing a mouse awake with the attached Si NN-patch on the skin.
Movie S5. A continuously recorded movie (scale bar, 2 cm; 1× speed) showing a mouse awake with the implanted Si NN-patch on the subcutaneous muscle.

REFERENCES AND NOTES

1. X. Duan, R. Gao, P. Xie, T. Cohen-Karni, Q. Qing, H. S. Choe, B. Tian, X. Jiang, C. M. Lieber, Intracellular recordings of action potentials by an extracellular nanoscale field-effect transistor. *Nat. Nanotechnol.* **7**, 174–179 (2011).
2. A. K. Shalek, J. T. Robinson, E. S. Karp, J. S. Lee, D.-R. Ahn, M.-H. Yoon, A. Sutton, M. Jorgolli, R. S. Gertner, T. S. Gujral, G. MacBeath, E. G. Yang, H. Park, Vertical silicon nanowires as a universal platform for delivering biomolecules into living cells. *Proc. Natl. Acad. Sci. U.S.A.* **107**, 1870–1875 (2010).
3. R. X. Yan, J.-H. Park, Y. Choi, C.-J. Heo, S.-M. Yang, L. P. Lee, P. D. Yang, Nanowire-based single-cell endoscopy. *Nat. Nanotechnol.* **7**, 191–196 (2012).
4. Z. Luo, Y. Jiang, B. D. Myers, D. Isheim, J. Wu, J. F. Zimmerman, Z. Wang, Q. Li, Y. Wang, X. Chen, V. P. Dravid, D. N. Seidman, B. Tian, Atomic gold–enabled three-dimensional lithography for silicon mesostructures. *Science* **348**, 1451–1455 (2015).
5. M. E. Spira, A. Hai, Multi-electrode array technologies for neuroscience and cardiology. *Nat. Nanotechnol.* **8**, 83–94 (2013).
6. M. Goldberg, R. Langer, X. Jia, Nanostructured materials for applications in drug delivery and tissue engineering. *J. Biomater. Sci. Polym. Ed.* **18**, 241–268 (2007).
7. C. Chiappini, E. De Rosa, J. O. Martinez, X. Liu, J. Steele, M. M. Stevens, E. Tasciotti, Biodegradable silicon nanoneedles delivering nucleic acids intracellularly induce localized in vivo neovascularization. *Nat. Mater.* **14**, 532–539 (2015).
8. C. Chiappini, J. O. Martinez, E. De Rosa, C. S. Almeida, E. Tasciotti, M. M. Stevens, Biodegradable nanoneedles for localized delivery of nanoparticles in vivo: Exploring the biointerface. *ACS Nano* **9**, 5500–5509 (2015).
9. X. Xie, A. Aalipour, S. V. Gupta, N. A. Melosh, Determining the time window for dynamic nanowire cell penetration processes. *ACS Nano* **9**, 11667–11677 (2015).
10. J. J. VanDersarl, A. M. Xu, N. A. Melosh, Nanostraws for direct fluidic intracellular access. *Nano Lett.* **12**, 3881–3886 (2012).
11. J. Abbott, T. Ye, L. Qin, M. Jorgolli, R. S. Gertner, D. Ham, H. Park, CMOS nanoelectrode array for all-electrical intracellular electrophysiological imaging. *Nat. Nanotechnol.* **12**, 460–466 (2017).
12. J. T. Robinson, M. Jorgolli, A. K. Shalek, M.-H. Yoon, R. S. Gertner, H. Park, Vertical nanowire electrode arrays as a scalable platform for intracellular interfacing to neuronal circuits. *Nat. Nanotechnol.* **7**, 180–184 (2012).
13. Z. Huang, H. Fang, J. Zhu, Fabrication of silicon nanowire arrays with controlled diameter, length, and density. *Adv. Mater.* **19**, 744–748 (2007).
14. R. Elnathan, L. Isa, D. Brodoceanu, A. Nelson, F. J. Harding, B. Delalat, T. Kraus, N. H. Voelcker, Versatile particle-based route to engineer vertically aligned silicon nanowire arrays and nanoscale pores. *ACS Appl. Mater. Interfaces* **7**, 23717–23724 (2015).
15. Y.-S. No, R. Gao, M. N. Mankin, R. W. Day, H.-G. Park, C. M. Lieber, Encoding active device elements at nanowire tips. *Nano Lett.* **16**, 4713–4719 (2016).
16. D. P. Brennan, A. Dobley, P. J. Sideris, S. R. J. Oliver, Swollen poly(dimethylsiloxane) (PDMS) as a template for inorganic morphologies. *Langmuir* **21**, 11994–11998 (2005).
17. D. P. Holmes, M. Roché, T. Sinha, H. A. Stone, Bending and twisting of soft materials by non-homogenous swelling. *Soft Matter* **7**, 5188–5193 (2011).
18. N. J. van de Berg, T. L. de Jong, D. J. van Gerwen, J. Dankelman, J. J. van den Dobbelsteen, The influence of tip shape on bending force during needle insertion. *Sci. Rep.* **7**, 40477–40484 (2017).
19. T. Ando, M. Shikida, K. Sato, Tensile-mode fatigue testing of silicon films as structural materials for MEMS. *Sens. Actuators A Phys.* **93**, 70–75 (2001).
20. H. T. Zhang, J. Tersoff, S. Xu, H. Chen, Q. Zhang, K. Zhang, Y. Yang, C.-S. Lee, K.-N. Tu, J. Li, Y. Lu, Approaching the ideal elastic strain limit in silicon nanowires. *Sci. Adv.* **2**, 1501382–1501389 (2016).
21. S. J. Pearton, T. Lele, Y. Tseng, F. Ren, Penetrating living cells using semiconductor nanowires. *Trends Biotechnol.* **25**, 481–482 (2007).
22. Y.-S. Park, S. Y. Yoon, J. S. Park, J. S. Lee, Deflection induced cellular focal adhesion and anisotropic growth on vertically aligned silicon nanowires with differing elasticity. *NPG Asia Mater.* **8**, e249 (2016).
23. R. Wierzbicki, C. Købler, M. R. B. Jensen, J. Łopacińska, M. S. Schmidt, M. Skolimowski, F. Abeille, K. Qvortrup, K. Mølhave, Mapping the complex morphology of cell interactions with nanowire substrates using FIB-SEM. *PLOS ONE* **8**, e53307 (2013).
24. R. Elnathan, M. Kwiat, F. Patolsky, N. H. Voelcker, Engineering vertically aligned semiconductor nanowire arrays for applications in the life sciences. *Nano Today* **9**, 172–196 (2014).
25. H. Han, Z. Huang, W. Lee, Metal-assisted chemical etching of silicon and nanotechnology applications. *Nano Today* **9**, 271–304 (2014).
26. S.-W. Hwang, H. Tao, D.-H. Kim, H. Cheng, J.-K. Song, E. Rill, M. A. Brenckle, B. Panilaitis, S. M. Won, Y.-S. Kim, Y. M. Song, K. J. Yu, A. Ameen, R. Li, Y. Su, M. Yang, D. L. Kaplan, M. R. Zakin, M. J. Slepian, Y. Huang, F. G. Omenetto, J. A. Rogers, A physically transient form of silicon electronics. *Science* **337**, 1640–1644 (2012).
27. L. Yin, A. B. Farimani, K. Min, N. Vishal, J. Lam, Y. K. Lee, N. R. Aluru, J. A. Rogers, Mechanisms for hydrolysis of silicon nanomembranes as used in bioresorbable electronics. *Adv. Mater.* **27**, 1857–1864 (2015).
28. S.-W. Hwang, G. Park, C. Edwards, E. A. Corbin, S.-K. Kang, H. Cheng, J.-K. Song, J.-H. Kim, S. Yu, J. Ng, J. E. Lee, J. Kim, C. Yee, B. Bhaduri, Y. Su, F. G. Omennetto, Y. Huang, R. Bashir, L. Goddard, G. Popescu, K.-M. Lee, J. A. Rogers, Dissolution chemistry and biocompatibility of single-crystalline silicon nanomembranes and associated materials for transient electronics. *ACS Nano* **8**, 5843–5851 (2014).
29. W. Zhou, X. C. Dai, T.-M. Fu, C. Xie, J. Liu, C. M. Lieber, Long term stability of nanowire nanoelectronics in physiological environments. *Nano Lett.* **14**, 1614–1619 (2014).
30. S. Y. Ryu, J. Xiao, W. I. Park, K. S. Son, Y. Y. Huang, U. Paik, J. A. Rogers, Lateral buckling mechanics in silicon nanowires on elastomeric substrates. *Nano Lett.* **9**, 3214–3219 (2009).
31. C.-L. Hsin, W. Mai, Y. Gu, Y. Gao, C.-T. Huang, Y. Liu, L.-J. Chen, Z.-L. Wang, Elastic properties and buckling of silicon nanowires. *Adv. Mater.* **20**, 3919–3923 (2008).

Acknowledgments: We thank K. Park for insightful comments on an earlier manuscript. **Funding:** C.H.L. acknowledges funding support from the Asian Office of Aerospace Research & Development (AOARD: FA2386-16-1-4105), the Air Force Office of Scientific Research (AFOSR: FA2386-18-1-40171), and the College of Engineering at Purdue University. D.R.K. acknowledges funding support from the International Research and Development Program (NRF- 2018K1A3A1A32055469) through the National Research Foundation of Korea (NRF) funded by the Ministry of Science and ICT of Korea, the Intelligent Synthetic Biology Center of Global Frontier Project (NRF-2012M3A6A8054889), and the Basic Science Research Program (NRF-2015R1C1A1A02037752) funded by the Ministry of Science and ICT of Korea. **Author contributions:** C.H.L. and D.R.K. designed the research. H.K., H.J., M.K.K., D.S.W., H.S.L., D.R.K., and C.H.L. performed the research. B.K. and C.H.L. performed the computational mechanical analysis. H.K., H.J., B.K., D.R.K., and C.H.L. wrote the paper. All authors analyzed the data and commented on the paper. **Competing interests:** D.R.K. and C.H.L. are inventors on a pending patent related to this work (serial no. 62/737,210; filed on 27 September 2018). The authors declare no other competing interests. **Data and materials availability:** All data needed to evaluate the conclusions in the paper are present in the paper and/or the Supplementary Materials. Additional data related to this paper may be requested from the authors.

Submitted 6 July 2018
Accepted 5 October 2018
Published 9 November 2018
10.1126/sciadv.aau6972

Citation: H. Kim, H. Jang, B. Kim, M. K. Kim, D. S. Wie, H. S. Lee, D. R. Kim, C. H. Lee, Flexible elastomer patch with vertical silicon nanoneedles for intracellular and intratissue nanoinjection of biomolecules. *Sci. Adv.* **4**, eaau6972 (2018).